# Revealing the hidden polysulfides in solid-state Na-S batteries: How pressure and electrical transport control kinetic pathways

Hung Quoc Nguyen[1], Mikael Dahl Kanedal[1], Juraj Todt[2], Feng Jin[1], Quyen Do[3], Dora Zalka[4], Alexey Maximenko[4], Dragos Stoian[5], Norbert Schell[6], Wouter van Beek[5], Steven T. Boles[3], Jozef Keckes[2], Daniel Rettenwander[1,7*]

[1] Department of Materials Science and Engineering, NTNU Norwegian University of Science and Technology, 7034 Trondheim, Norway

[2] Chair of Materials Physics, Montanuniversität Leoben and Erich Schmid Institute for Materials Science, Austrian Academy of Sciences, Leoben 8700, Austria

[3] Department of Energy and Process Engineering, Norwegian University of Science and Technology, Trondheim 7491, Norway

[4] National Synchrotron Radiation Centre SOLARIS, Jagiellonian University, Czerwone Maki 98, 30-392, Kraków, Poland

[5] Swiss-Norwegian Beamlines, European Synchrotron Radiation Facility, 71 Ave. des Martyrs, Grenoble 38000, France

[6] Helmholtz-Zentrum Hereon, Max-Planck-Straße 1, 21502 Geesthacht, Germany

[7] Christian Doppler Laboratory for Solid State Batteries, Norwegian University of Science and Technology, 7034 Trondheim, Norway

[*] Corresponding author: daniel.rettenwander@ntnu.no

## Abstract

*Room temperature operation of Na-S batteries with liquid electrolytes is plagued by fundamental challenges stemming from polysulfide solubility and their shuttle effects. Inorganic solid electrolytes offer a promising solution by acting as barriers to polysulfide migration, mitigating capacity loss. While the sequential formation of cycling products in molten-electrode and liquid electrolytes-based Na-S batteries generally aligns with the expectations from the Na-S phase diagram, their presence, stability, and transitory behavior in systems with inorganic solid electrolytes at room temperature, remain poorly understood. To address this, we employed operando scanning micro-beam X-ray diffraction and ex-situ X-ray absorption spectroscopy to investigate the sulfur conversion mechanisms in Na-S cells with $Na_3PS_4$ and $Na_4(B_{10}H_{10})(B_{12}H_{12})$ electrolytes. Our findings reveal the formation of crystalline and amorphous polysulfides, including those predicted by the Na-S phase diagram (e.g., $Na_2S_5$, $Na_2S_4$, $Na_2S_2$, $Na_2S$), high-order polysulfides observed in liquid-electrolyte systems (e.g., $Na_2S_x$, where x = 6–8), and phases like $Na_2S_3$ typically stable only under high-temperature or high-pressure conditions. We demonstrate that these transitions are governed by diffusion-limited kinetics and localized stress concentrations, emphasizing the critical role of pressure, which serves as both a thermodynamic variable, as well as a design parameter, for optimizing solid-state Na-S battery performance necessary for pushing these cells closer to the commercial frontier.*

*Keywords: sodium-sulfur battery, polysulfides, solid-state, operando XRD*

# 1. Introduction

Na–S batteries, despite their relatively limited commercial deployment in recent years, have a substantial history in mobile energy storage, primarily due to their high energy density, abundance of sodium and sulfur, and potential for cost-effectiveness.[1] Before the rise of lithium-based chemistries and sustainability-driven policies, Na–S cells held promise across sectors, notably in the global automotive industry. This promise was bolstered by the low melting points of Na and S and the discovery of rapid Na-ion transport in β"-alumina, which catalyzed interest in liquid-electrode systems.[2] However, recent advances in room-temperature-compatible aprotic electrolytes have revived the interest in Na–S batteries that function at ambient temperatures.[3]

Recent Na–S systems with heavily 'cocktail'-optimized liquid electrolytes have exhibited impressive performance, showing an initial capacity of 1635 mAh/g (sulfur weight basis) at 0.1C, with 56.7% capacity retention over 200 cycles and high coulombic efficiency.[4] However, even these advancements fall short of the high-performance criteria required for large-scale energy storage and mobility applications, particularly given the 10+ year lifespans now standard for conventional Li-ion batteries.[5] This raises the question of whether electrolyte engineering alone can overcome the fundamental challenges inherent in sulfur-cathode cells, such as (i) polysulfide dissolution and shuttle effects and (ii) significant volume changes during redox cycling, both of which contribute to chemo-mechanical degradation at the cathode–electrolyte interface. The analogous Li–S battery system has faced similarly challenges, prompting growing research efforts to optimize the cathode structure and interface for enhanced compatibility with liquid electrolytes.[6-8]

An alternative approach involves integrating inorganic solid electrolytes, which could intrinsically address polysulfide sodiation reversibility.[9] The particulate morphology of solid-state materials, combined with carbon-black mixing, constrains sulfur hosts within a stable position, removing some of the risks associated with dissolution. This stability contrasts with liquid systems, where electrolyte fluid mechanics makes dissolution catastrophic. In liquid cells, a complex "solid-liquid-solid" transformation occurs during cycling, involving long-chain (soluble) and short-chain (non-soluble) polysulfides with characteristic discharge plateaus.[10] In solid-state Na–S cells, however, the physical stability and variable stack pressure of solid components provide a different, albeit challenging, chemo-mechanical environment, which is similar to the Li-S cells.[11, 12] Mechanisms for transforming S to $Na_2S$ in solid systems are anticipated to resemble those in liquid and molten Na–S cells  but with unique kinetic

2

dynamics. Observations of solid-solid reactions in solid-state Na–S batteries hint at similar behaviors, though the existence of polysulfide intermediates remains poorly understood (see Figure 1a,b).[9]

In a departure from this challenge, Tanibata et al. reveal multi-plateau discharge profiles in all-solid-state Na–S cells, with the initial formation of amorphous sodium polysulfides ($Na_2S_x$) followed by conversion to crystalline $Na_2S$.[13] This finding suggests a complex reaction mechanism with untapped potential for enhancing sodium-sulfur battery performance. The reversibility operation of Na–S cells depend critically on the nature (chemical and mechanical) of the phase transitions between $Na_2S$ and S.

In this study, we elucidate the complex sulfur conversion mechanism in solid-state Na-S cells with $Na_3PS_4$ (NPS) and $Na_4(B_{10}H_{10})(B_{12}H_{12})$ (NBH) electrolytes using operando scanning micro-beam X-ray diffraction and ex-situ soft X-ray absorption spectroscopy. These techniques enable a detailed examination of the polysulfide evolution, phase transitions, and associated stress dynamics within the cell during operation. We reveal that both crystalline and amorphous polysulfides are formed from solid-state reactions. They include (i) the polysulfides identified in the Na-S phase diagram ($Na_2S_5$, $Na_2S_4$, $Na_2S_2$, and $Na_2S$), (ii) high-order polysulfides previously reported in Na–S batteries with liquid electrolytes ($Na_2S_x$, where x = 6–8), and (iii) $Na_2S_3$, which emerges only at high temperature or high-pressure conditions. These transformations are governed by diffusion-limited kinetics and localized stresses. Beyond elucidating the full Na–S reaction pathway, this work emphasizes the critical role of pressure as a thermodynamic variable in exploring reaction mechanisms while also shaping reaction pathways, which offers new perspectives for optimizing solid-state battery performance.

## 2. Results and Discussions

To reveal the reaction mechanism of S in solid-state Na-S batteries, we performed operando scanning micro-beam X-ray diffraction along the cross-section of the cell. This technique not only allows tracking of phases and microstructural changes but also the associated stress evolution in real-time. For performing the operando experiment, solid-state Na-S batteries have been assembled using a blend of $Na_{15}Sn_4$ (80%) and C (20%) as the anode, NPS as the separator, and a blend of S (33%), C (17%), and NPS (50%) as the composite cathode (areal loading: 3.6 mAh/cm$^2$). Details on preparation, assembly, and basic characterization related to materials and cell components are provided in Supplementary Note 1. Due to time constraints

at the synchrotron testing facility, conditions for cell testing need to be chosen to allow cell cycling without losing its electrochemical characteristics. For a current density of 50 mA/g, an initial discharge capacity of 1376.4 mAh/g has been achieved, comparable to previous reports for solid-state Na-S batteries operated at intermediate temperatures.[14] Interestingly, the voltage profile and differential capacity plot indicate distinct electrochemical signatures that are mostly consistent with those previously reported for conventional Na-S batteries,[15] already strongly suggesting the prevalence of a multi-step reaction mechanism. When 100 mA/g was applied, the discharge capacity dropped to 1249 mAh/g (Supplementary Figure 2). As a higher current is applied, the drop in capacity comes naturally, along with an increasing overpotential, while the shape of the charge-discharge curves remains similar (Figure 1c). This indicates that a current density of 100 mA/g has no significant impact on the fundamental characteristics of the composite cathode; hence, this condition has been used for the operando experiments.

After identifying the optimal conditions to run the solid-state Na-S battery at the synchrotron, cells were assembled in a self-constructed operando device (Supplementary Figure 4), which allows experiments to be performed along the cross-section of the whole cell at constant pressure and temperature. The spatial and time evolution of observed phases in the diffraction experiment during charge and discharge, together with the corresponding voltage profile, are shown in Figure 2a. Details about the phase analysis can be found in Supplementary Note 2. In Figure 2b, the differential capacity (dq/dV) curve is shown in combination with thickness changes in the composite cathode layer and the overall compositional changes. Details about the refinement of diffraction data and their evaluation can be found in the experimental section and Supplementary Note 2.

Due to the preparation by high-energy ball milling, crystalline S transforms into its amorphous phase in the as-synthesized composite cathode.[13] Initially, a minor amount of crystalline sulfur (Figure 2a) and NPS (Supplementary Figure 3) can be identified in the diffraction pattern. There is no indication of any phase change that could be associated with the electrochemical signature observed during discharge up to ca. 6 h (1.27 V), while the peak at 7.5 h (1.17 V) can be assigned to the formation of $Na_2S$. The reversed reaction peak in the dq/dV plot at about 16h can be assigned to the desodiation reaction of crystalline $Na_2S$ (pink line) to crystalline $Na_2S_2$ (purple line). Consequently, we hypothesize that the reverse reaction takes place at about 16 h (1.84 V) due to the symmetrical shape for $Na_2S$ (assuming similar diffusion-controlled reaction kinetics for both reaction directions). Since the refined quantity of $Na_2S$ does not match that of the converted $Na_2S_2$ during charge, we assume that $Na_2S_2$ underwent a partial amorphization (about 15 to 20 %). Since no further crystalline (poly)sulfur

4

species can be observed when further charging takes place, we assume a full amorphization of the polysulfides towards the formation of $S_8$.

The first peak in the dq/dV plot might be associated with the reversible decomposition of NPS.[16, 17] Although it appears reasonable at first glance due to the thermodynamic instability of NPS in the operated voltage range, the phase plots do not show any intensity loss that could support this conclusion (Supplementary Figure 3). Instead, if this plateau is not related to the electrolyte redox chemistry, the question arises: What does it belong to? We hypothesize that other polysulfides, amorphous in nature, could have been formed as an additional intermediate reaction step. This is reasonable, considering the similar shape of the voltage profile to that of conventional Na-S batteries (Figure 1c).

To identify the presence of missing polysulfides, we performed ex-situ XAS on identical cells, as this approach allowed us to track both crystalline and amorphous compounds. To avoid sulfur species interference from NPS, we used a closo-borate electrolyte (NBH) in cell assembly (see experimental section for further details). Replacing NPS with NBH alters the shape of the dq/dV plot (due to the better ionic transport of NBH), though the obvious electrochemical features remain comparable (Figure 3a). Despite the notable difference around 1.7–1.8 V marked by an additional contribution, closer inspection indicates that the most intense peak at 1.8 V (NBH) could be a superposition of peaks at ~1.7 and ~1.8 V. The merging of peaks could be related to the use of the higher Na-ion conductive NBH instead of NPS at given temperatures, indicating a rate-dependency of the conversion reactions. The rate-dependency and associated alterations of electrochemical signatures might also explain the controversial discussion about the reaction mechanism previously.[16] Moreover, the change of electrolyte also further supports our hypothesis that the minor peak at the beginning of discharge cannot be associated with NPS decomposition. Besides, the battery cell with NBH electrolyte achieved high capacity and good cycling performance even at a high rate of 500 mA/g at 30 °C (Figure 3e).

To explore potential reaction steps, multiple cells were assembled and cycled to characteristic features in the voltage profile, i.e. 0.5, 1.0, 1.1, 1.2, 1.3, 1.5, 1.7, 1.8, and 1.9 V, as well as 2.8, 2.3, 2.2, 2.1, 2.0, 1.9, 1.8, 1.75, 1.7, 1.6 and 1.5 V. The corresponding spectra and analysis are shown in Figure 3b (map), Figure 3c-d (quantitative analysis), and Supplementary Figure 5 (line scan). Details about the spectral fitting and analysis can be found in Supplementary Notes 3 and Supplementary Figure 6. The XAS spectra initially resemble those of α-S (elemental sulfur) and a polymeric $S_8$ composite. Upon discharge from OCV to 1.9 V, the primary sulfur feature at 2471.5 eV diminishes, while a shoulder at 2469.5 eV,

5

attributed to negatively charged terminal sulfur atoms, becomes apparent. It is a marker for the conversion of $S_8$ to long-chain polysulfides. The intensity of this shoulder peak at 1.9 V suggests that x in $Na_2S_x$ exceeds 7, indicating the presence of a mixture of polysulfides with x $\geq$ 6. This agrees with previous reports using in-situ TEM on a Na-S nanobattery. They found the formation of amorphous polysulfides with x $\geq$ 6; a clear assignment to either $Na_2S_6$, $Na_2S_7$, or $Na_2S_8$ was, however, not possible.[18] By continuing discharging to 1.8 V, the intensity analysis of the two main features of sulfur shows x ~ 5. Therefore, at this voltage, $Na_2S_5$ is the dominating product. Discharging to 1.7 V marks the existence of $Na_2S_4$. The shoulder peak dominates as discharge continues, reaching maximum intensity at shorter-chain polysulfides. At 1.5 V cut-off voltage, the analysis shows $Na_2S_3$ as the discharge product. Simultaneously, the primary sulfur feature continues to fade. These observations call to mind those reported for high-temperature solid-state Na-S batteries employing β′′-alumina (300 °C). Similar electrochemical signatures have been obtained and assigned to $Na_2S_5$, $Na_2S_4$, and $Na_2S_3$.[19]

Interestingly, this study clearly identified $Na_2S_3$, which is metastable under ambient conditions and decomposes to $Na_2S_2$ and $Na_2S_4$. Compared to $Na_2S_2$ and $Na_2S_4$, $Na_2S_3$ has a low formation enthalpy (4.1 meV/atom) and a stabilizing pressure of 900 MPa, suggesting that $Na_2S_3$ potentially forms when high enough pressure is applied.[20] This pressure phase sensitivity explains previous success in synthesizing $Na_2S_3$ at temperatures and pressures of about 30 °C and 200 MPa, respectively.[21] We hypothesize that $Na_2S_3$ can also form in solid-state Na-S batteries when high enough (local) pressure is generated due to the applied stack pressure or significant volume changes associated with the conversion reaction within the composite cathode.

To test this hypothesis, stress evolution associated with polysulfide formation was extracted from diffraction data (Methods; Supplementary Note 2). Given the amorphous nature of most polysulfides, stress was analyzed using NPS as a kind of internal stress sensor. A complex stress profile emerged within the composite cathode (Figure 4a), driven by conversion reactions and substantial volume changes. These phase transformations and associated volume changes are evident from the regions of diminished and augmented intensity peak intensity maps of $Na_2S$, $Na_2S_2$, and NPS (Figure 2a and Supplementary Figure 3). The composite cathode, i.e., sulfur species, expands during discharge, effectively compressing the separator and anode and vice versa during charge (Supplementary Note 2 regarding stress analysis). These behaviors are predominantly linked to the $Na_2S_2$-to-$Na_2S$ conversion process, with other reactions contributing negligibly. Measured stress profiles revealed increasing tensile deviatoric stresses in both the parent NPS and newly formed $Na_2S$ phases, peaking at 280 MPa and 180 MPa,

6

respectively, near full discharge. This phenomenon may be explained by a predominantly compressive radial stress component and a tensile axial component, consistent with $Na_2S$ finally precipitating in needle- or leaf-like morphologies within the $Na_3PS_4$ matrix, oriented parallel to the thickness of the cell (Supplementary Note 2). Indeed, such morphologies have been observed in conventional Li–S system.[22, 23]

Despite the anisotropic stress distribution, the high average axial stress (~300 MPa) during cell operation supports the proposed stabilization of $Na_2S_3$ under high-pressure conditions. This highlights the critical role of pressure in solid-state batteries on the reaction mechanism, which could significantly impact cell performance.

Moreover, unlike the recent report proposing that $Na_2S_2$ is thermodynamically unstable (based on the presence of $Na_2S_2$ in ex-situ XAS measurements but its absence in in-situ Raman studies),[16] we observe this phase in both operando XRD (see above) and ex-situ XAS. The observation is again in good agreement with in-situ TEM studies of nano Na-S batteries at high and intermediate temperatures, showing that $Na_2S_2$ is a product of the conversion process, even at fast charging conditions.[18] Between 1.5 and 1.2 V, the main $S_8$ feature finally diminishes, while the contribution from short chain polysulfides further increases. By 1.1 V, $Na_2S_2$ becomes the dominant spectral contributor. At 1.0 V, while some spectral distortion persists, $Na_2S_2$ and $Na_2S$ appear as primary contributors, potentially alongside longer polysulfides. At the end of discharge, $Na_2S$ is the main discharge product existing with other $Na_2S_x$ species as the average x is nearly 1, (though not exactly unity). It is worth noting that the coexistence is expected as the discharge capacity does not reach the theoretical capacity of sulfur. The final conversion step, i.e., $Na_2S_2$ to $Na_2S$, provides half of the capacity of the battery, but is also associated with the slowest kinetics among polysulfides, making them rate limiting (the slower kinetics also explain the more significant shift of the peak in the dq/dV plot).[24-26] Due to the rate-limiting nature of $Na_2S_2$ formation and similar $\Delta G$ values, it has been suggested that $Na_2S$ forms directly from $Na_2S_4$ at kinetics-limited conditions.[16] However, distinct peaks from the dq/dV curves of the discharge process, even at high cycling rates, low temperatures, and for electrolytes with different ionic conductivities, can still be observed. Previous studies might have not considered those peaks as significant due to low intensity (note, some peaks have only a tenth of the main peak based on the contributing capacity). Based on our observations and finding for high-temperature Na-S batteries,[18, 19] we conclude that during discharge, sulfur undergoes a sequential conversion to $Na_2S_x$, with x = 6 to 8, $Na_2S_5$, $Na_2S_4$, $Na_2S_3$, $Na_2S_2$, and $Na_2S$.

During charging, from 1.5 to 1.75 V (like 1.3–1.2 V during discharge), the shoulder peak intensifies, with position shifts suggesting low-order polysulfides with a dominant contribution from $Na_2S_2$ (similar to 1.3 to 1.0 V during discharge). As the spectra clarify at higher voltages, more detailed interpretations become possible. At 1.8 V, the spectral profile reflects a mixture of low- and high-order polysulfides similar to 1.5 V during discharge which have been attributed herein to $Na_2S_5$, $Na_2S_4$, and $Na_2S_3$. From 1.8 to 2.3 V, the shoulder feature steadily decreases in intensity, while the $S_8$ peak shows continuous growth. Although this feature diminishes, it remains faintly detectable up to 2.8 V. At 2.8 V, with most polysulfides converted to $S_8$, the spectra do not fully match the pristine state. This observation mirrors findings in Li-S systems. In the Li system, sluggish solid-solid reaction kinetics and low ionic conductivity limit of full utilization of $S_8$, resulting in a final discharge product composed of $Li_2S$, $Li_2S_2$, and residual $S_8$.[27, 28] During charging, $Li_2S_2$ partially resists reoxidation to $S_8$. We observe a similar phase evolution in the sodium system, especially in the cross-sectional phase composition (Figure 2b, bottom). However, we question the previously suggested coexistence of polysulfides[28] e.g., $Na_2S$ and $Na_2S_2$ (but also $Li_2S$ and $Li_2S_2$) thought to result from slow polysulfide redox reactions. This view largely comes from bulk characterization techniques, which may obscure the actual reaction mechanisms by averaging the composition across the entire cathode. We did not observe both phases coexisting at the same location along the cathode cross-section.

Our findings reveal that new phases initiate formation at the separator|cathode interface and progressively propagate toward the current collector. This behavior can be attributed to the evolution of SOC gradients in solid-state batteries, which are linked to the electrical potential gradient across the composite cathode arising from kinetic limitations. This gradient results in an overpotential, which is lowest at the separator|cathode interface, driving the onset of reaction evolution at this location.[29, 30] This suggest that the incomplete utilization of sulfur is not due to limitations in its redox chemistry but rather to the operational voltage range of the cell is insufficiently broad to accommodate the rising overpotential across the composite cathode.

Regarding $Na_2S_4$, it has been suggested that it forms directly from $Na_2S$ during charging at kinetic-limited conditions.[16] However, this contrasts with evidence in our work: we observe that changes in kinetics lead to peak merging, as highlighted by the blue peaks in Figure 3a, rather than their disappearance. Further investigation of rate dependency in dq/dV plots, as seen in Figure 3f, shows both increased polarization with higher current densities and merging of peaks. The increasing polarization can be connected to the diffusion limitation in the 2D cathode plane, causing a polarization gradient in vertical space. This kinetic limitation with

8

increased rate causes polysulfide formations to overlap. The kinetic limitation in the Na-S cathode becomes more apparent with temperature change, shown in the cyclic voltammogram in Figure 3g. At higher temperatures, the formation peaks become more distinct and separated, showing the enhancement from improved kinetics and diffusion.

## 3. Conclusion

Solid-state Na–S batteries are gaining renewed attention as a promising energy storage technology, offering high energy density, enhanced safety, and cost-effectiveness due to the abundance of sodium and sulfur. Despite their potential, the conversion-reaction pathway of sulfur with sodium in solid-state systems employing an inorganic electrolyte remains poorly understood. In this work, we employ operando scanning micro-beam X-ray diffraction and ex-situ soft X-ray absorption spectroscopy to elucidate the multi-step evolution of sodium polysulfides. We uncover the formation of both crystalline and amorphous polysulfides, including species predicted by the Na-S phase diagram ($Na_2S_5$, $Na_2S_4$, $Na_2S_2$, $Na_2S$), high-order polysulfides observed in liquid-electrolyte systems ($Na_2S_x$, where x = 6–8), and phases such as $Na_2S_3$ typically stable only under high-temperature or high-pressure conditions (The mechanism is summarized in Figure 4b). Beyond elucidating the full Na–S reaction pathway, this work also emphasizes the critical role of pressure as a thermodynamic variable in exploring reaction mechanisms and shaping them, offering new perspectives for optimizing solid-state battery performance.

9

# 4. Experiment section

## 4.1 Materials preparation

***Synthesis of Na₃PS₄ (NPS).*** *Synthesis of $Na_3PS_4$ (NPS).* NPS, as the solid electrolyte, was synthesized using a high-energy ball-milling procedure and a subsequent annealing process, as previously reported.[31] Specifically, $Na_2S$ (Fisher Scientific 96.18%) and $P_2S_5$ (Sigma Aldrich 99%) were weighed with stoichiometric molar ratio (3:1) and mechanically mixed in a $ZrO_2$ container with $ZrO_2$ balls (diameter =10 mm, ball to powder weight ratio=28.3:1) in a planetary ball mill (Retsch PM100) at 550 rpm for 3 h. The obtained powder was pelletized (at 150 MPa) and further annealed at 270 °C with a heating rate of 10 °C/min for 2 h in Ar atmosphere.

***Synthesis of Na₄(B₁₀H₁₀)(B₁₂H₁₂) (NBH):*** *Synthesis of $Na_4(B_{10}H_{10})(B_{12}H_{12})$ (NBH):* NBH, as the solid electrolyte, was synthesized by high-energy ball-milling and a subsequent annealing process, as reported previously[32]. Precursors, $Na_2B_{10}H_{10}$ and $Na_2B_{12}H_{12}$, were weight and further mixed in a $ZrO_2$ container with an equimolar ratio (1:1) in a planetary ball mill at 500 rpm for 2 h. Then, the mixed powder was pelletized under 100 MPa and annealed at 270°C under dynamic vacuum for 12 hours. The annealed material was pulverized in an agate mortar and further ball milled for 24 h at 660 rpm before using.

***Forming Sodium-Tin alloy.*** Na and Sn with a stoichiometric molar ratio of 15:4 were added together with 20% carbon (Ketjen Black) in a ball milling jar and further sealed under Argon (Ar) atmosphere. Then, the mechanical alloying was performed for 4 h under 500 rpm, as elucidated by Tanibata et al.[33]

***Preparation of cathode composites.*** A two-step procedure was conducted to prepare the cathode composite for the all-solid-state Na-S batteries. In the first step, one gram mixture of Sulfur and carbon (2:1 in weight ratio, respectively) was homogeneously hand-mixed with a weight ratio of 2:1 in an agate mortar for 30 minutes and further planetarily mixed for 30 minutes at 2000 rpm. Then, the S/C mixture and NPS were further mixed with a weight ratio of 1:1 for 4 h at 500 rpm to obtain the cathode composite. All of the processes were conducted in an Ar atmosphere. The mass ratio in the obtained cathode composite is 3:1:2 for NPS, C, and S, respectively.

## 4.2 Physicochemical characterizations

***Thermal Gravimetric Analysis (TGA)***. TGA test was conducted on a STA 449 F3 Jupiter thermal analyzer (Netzsch) within a temperature range of room temperature (21 ºC) to 600 ºC with the ramping rate of 10 ºC/min under Ar atmosphere.

***X-ray diffraction.*** samples were loaded into a 10 mm diameter silicon cavity sample support (zero diffraction) and sealed with a dome holder (Bruker) made from polyacrylate to avoid exposure to the ambient environment. The XRD patterns were collected with a 2θ range of 10-70° and a sample rotation speed of 30 rpm on a Bruker D8 Advance goniometer equipped with a Bruker LYNXEYE detector using Cu Kα radiation.

For operando synchrotron X-ray diffraction, the cells have been assembled in a modified custom-made solid-state cell (Supplementary Figure 4). To begin with, 8 mg of NPS was loaded into the cell cold-pressed at approximately 380 MPa for 3 minutes. After that, 0.5 mg of cathode composite and 9 mg of alloy anode composite were inserted into different sides of the cells. Finally, the cell was pressed under 150 MPa for 3 minutes for compacting. A stack pressure of roughly 50 MPa was applied during the charge-discharge process. A controlling system employing a piezo was used to ensure constant stack pressure during cycling.

***Scanning micro-beam X-ray diffraction.*** Diffraction experiments were carried out at the high energy materials science beamline (HEMS) side-station P07b operated by Helmholtz Zentrum Hereon at the PETRA III synchrotron of DESY in Hamburg, Germany. A monochromatic X-ray beam with a photon energy of 87.1 keV and lateral dimensions of 500 μm horizontally and 10 μm vertically was scanned repeatedly across the entire stack of cell layers using a scanning step size of 10 μm over a distance of 1 mm, and a resulting scanning period of 0.5 hours. This acquisition scheme resulted in an effective thickness-position vs. discharge/charge time mapping of the cell. Powder-like diffraction patterns were collected for each mapped point in transmission on a Perkin Elmer XRD 1621 Flat Panel area-sensitive X-ray detector with an effective resolution of 2048 x 2048 pixels, placed 1481 mm downstream of the sample. The exact detector geometry with respect to the gauge volume was calibrated by measuring a NIST $LaB_6$ standard powder and employing the routines provided by the pyFAI software package.[34, 35] The mapping of the evolution of phase (trans)formations was carried out by integrating the intensities of specific visible reflections within a narrow range of diffraction angle 2θ conceptionally equivalent to annular dark-field contrast in a TEM. Additionally, localized background subtraction was performed from within the neighborhood of the specifically investigated reflections, improving the signal/noise ratio for weakly scattering phases. As in the stress evaluation, averaging multiple reflections also served to improve reliability for some phases, applying this approach for 211 and 220 of cubic $Na_{15}Sn_4$, 110 of cubic $Na_3PS_4$, 111, 220 and 422 of cubic $Na_2S$, 200 of rhombohedral $Na_2S_2$ and 113 of orthorhombic S. The resulting peak intensity maps show the presence of a phase (in arbitrary

units) with respect to time and the thickness position in the cell. In the case of $Na_2S$, this also contains some spurious signals where some reflection of another phase overlaps in a different part of the cell.

The measurements of powder samples as reference were performed at beamline BM01 at the Swiss-Norwegian beamlines at the European Synchrotron Radiation Facility. A small amount of sample was loaded into a quartz capillary (Hilgenberg GmbH) and sealed with wax prior to measurement. Beam size of $150 \times 300$ μm$^2$ with a wavelength of 0.78242 Å, and a two-dimensional (2D) detector (2M Pilatus) were used. The data was integrated by using Bubble software.[36] The precise detector position was calibrated by measuring a standard silicon reference powder, utilizing the module provided by the pyFAI software package.[35]

**Ex-situ tender-X-ray absorption spectroscopy (XAS)**. Samples of the sulfur cathode were prepared by discharging and charging the cell to different cut-off voltages. Sulfur K-edge XANES (short energy scans around the S K-edge absorption line) spectra were collected in a transition mode at ASTRA beamline at the SOLARIS National Synchrotron Radiation Center (Krakow, Poland). Athena software (part of the Demeter package) was used to process the raw data (calibration, normalization, background subtraction) and to extract the XANES signal further used for plotting and interpretation (detailed description in Supplementary Note 3).[37] A $ZnSO_4$ scan was performed between any two separate measurements, and they served as standards for energy calibration. To this end, all the first derivative maxima from the zinc sulfate references were previously aligned to 2480.5 eV to extract the energy shift (correction) to be applied to the sample spectra. No deviation larger than +/- 1 eV was ever observed. While we measured using both transmission and fluorescence geometries, the former was preferred since we could prepare decent thickness samples that resulted in workable transmission spectra; in this way, we could avoid all the possible interferences linked to the over-absorption in fluorescence, and the quantification would have been more difficult to tackle – hence limiting us to a more qualitative analysis.

### 4.3 Electrochemical characterization

**Electrochemical impedance spectroscopy (EIS):** The ionic conductivity of the as-synthesized solid electrolyte material was evaluated by EIS. The electrolyte pellet was formed by using a PEEK die mold with stainless steel plungers (TCH Instruments). 80 mg of NPS powder was loaded into the 10 mm diameter PEEK pellet die and pressed at around 380 MPa (3000 kgf) at room temperature for 3 minutes. Thin carbon layers were introduced between the pellet and the two stainless steel plungers as current collectors for the EIS measurements. Data

12

was collected with a Biologic VMP300 potentiostat, with an excitation potential of 10 mV and a frequency range between 7 MHz and 1 Hz. During the measurement, the sample was put under 50 MPa constant pressure. A special solid-state cell from RHD Instruments was used for the temperature-dependent test. In detail, 115 mg NPS powder was loaded into the 12 mm PEI pellet die and pressed at around 380 MPa at room temperature for 3 minutes. Two WC plungers were used as a current collector for the EIS measurement. After that, the cell was placed into a CompreDrive instrument for controlling the temperature under 50 MPa constant load. At each temperature, the cell was relaxed for two hours before EIS measurement. The EIS data was recorded with a Zahner IMex6 potentiostat with an excitation potential of 20 mV and a frequency range between 3 MHz and 1 Hz. The EIS spectra were analyzed by RelaxIS 3 (RHD Instruments).

*Galvanostatic cycling.* The cycling tests were performed with a total cathode loading of 5 mg ($6.36 \text{ mg/cm}^2$), corresponding to a sulfur loading of 1.65 mg ($2.10 \text{ mg/cm}^2$). In all batteries, cells were constructed by three layers. 80 mg of as-synthesized NPS ($101.86 \text{ mg/cm}^2$) was firstly loaded and compressed for 3 minutes inside the PEEK cell under 380 MPa using a Specac Atlas hydraulic press. After that, 5 mg of the cathode composite was loaded on one side of the pellet, and 100 mg $Na_{15}Sn_4$-C composite anode was loaded on the other side of the pellet. The three-layer cell was compressed under 150 MPa for 3 minutes for compacting. The cells were kept in a home-made frame with applied stack pressure of 50 MPa (by screwing the three nuts with 5 Nm torque force using a torque wrench) prior to cycling. The applied current for cycling was 164.93 µA ($210 \text{ µA/cm}^2$), corresponding to 100 mA/g. The lower and upper cutoff potentials were 0.5 V and 3.0 V. The galvanostatic charge-discharge cycling was performed using a Netware BTS4000 cycler controlled by BTS 8.0 software. All cycling tests were performed inside the Memmert UN30 high-temperature chamber at 80 °C. The capacity of the battery is calculated based on the mass of sulfur.

*Electrochemical testing in operando study.* *Galvanostatic charge-discharge.* Prior to measurement, the cell was heated up to 80 °C and the temperature was kept constant. During the operando measurement, the cell was cycled using a PalmSens4 potentiostat with a current density of $210 \text{ µA/cm}^2$ corresponding to 100 mA/g. The data was recorded using PSTrace 9.0 software. A dedicated experimental set-up was developed, allowing for operando cross-sectional scanning of model-type battery cells.

**Authors contribution**

H.N. and D.R. designed the experimental work. H.N., Q.D., S.T. and M.K. performed the in-house experiments. H.N., J.T., F.J., and N.S. performed the operando experiment at P07B beamline. A.M., D.S., D.Z., and W.B. perform the XAS experiment at ASTRA beamline. J.T. and J.K. analyzed the XRD Synchrotron data. D.R. supervised the work. All authors reviewed the results and approved the final version of the manuscript.

## Data Availability

The data that support the findings of this study are available from the corresponding author on reasonable request.

## Acknowledgment

## Competing interests

The authors declare no competing interests.

## References

(1) Hiremath, M.; Derendorf, K.; Vogt, T. Comparative life cycle assessment of battery storage systems for stationary applications. *Environmental science & technology* **2015**, *49* (8), 4825-4833.
(2) Hueso, K. B.; Armand, M.; Rojo, T. High temperature sodium batteries: status, challenges and future trends. *Energy & Environmental Science* **2013**, *6* (3), 734-749.
(3) Wang, Y. X.; Zhang, B.; Lai, W.; Xu, Y.; Chou, S. L.; Liu, H. K.; Dou, S. X. Room-temperature sodium-sulfur batteries: a comprehensive review on research progress and cell chemistry. *Advanced Energy Materials* **2017**, *7* (24), 1602829.
(4) Xu, X.; Zhou, D.; Qin, X.; Lin, K.; Kang, F.; Li, B.; Shanmukaraj, D.; Rojo, T.; Armand, M.; Wang, G. A room-temperature sodium–sulfur battery with high capacity and stable cycling performance. *Nature communications* **2018**, *9* (1), 3870.
(5) Masias, A.; Marcicki, J.; Paxton, W. A. Opportunities and challenges of lithium ion batteries in automotive applications. *ACS energy letters* **2021**, *6* (2), 621-630.

(6) Yu, X.; Manthiram, A. Electrode–electrolyte interfaces in lithium–sulfur batteries with liquid or inorganic solid electrolytes. *Accounts of chemical research* **2017**, *50* (11), 2653-2660.

(7) Zheng, Z.-J.; Ye, H.; Guo, Z.-P. Recent progress on pristine metal/covalent-organic frameworks and their composites for lithium–sulfur batteries. *Energy & Environmental Science* **2021**, *14* (4), 1835-1853.

(8) Liu, F.; Lu, W.; Huang, J.; Pimenta, V.; Boles, S.; Demir-Cakan, R.; Tarascon, J.-M. Detangling electrolyte chemical dynamics in lithium sulfur batteries by operando monitoring with optical resonance combs. *Nature Communications* **2023**, *14* (1), 7350.

(9) Ma, J.; Wang, M.; Zhang, H.; Shang, Z.; Fu, L.; Zhang, W.; Song, B.; Lu, K. Toward the Advanced Next-Generation Solid-State Na-S Batteries: Progress and Prospects. *Advanced Functional Materials* **2023**, *33* (20), 2214430.

(10) Jin, F.; Wang, R.; Liu, Y.; Zhang, N.; Bao, C.; Li, D.; Wang, D.; Cheng, T.; Liu, H.; Dou, S. Conversion mechanism of sulfur in room-temperature sodium-sulfur battery with carbonate-based electrolyte. *Energy Storage Materials* **2024**, *69*, 103388.

(11) Fujita, Y.; Münch, K.; Asakura, T.; Motohashi, K.; Sakuda, A.; Janek, J. r.; Hayashi, A. Dynamic volume change of Li2S-based active material and the influence of stacking pressure on capacity in all-solid-state batteries. *Chemistry of Materials* **2024**, *36* (15), 7533-7540.

(12) Ohno, S.; Zeier, W. G. Toward practical solid-state lithium–sulfur batteries: challenges and perspectives. *Accounts of materials research* **2021**, *2* (10), 869-880.

(13) Tanibata, N.; Deguchi, M.; Hayashi, A.; Tatsumisago, M. All-solid-state Na/S batteries with a Na3PS4 electrolyte operating at room temperature. *Chemistry of Materials* **2017**, *29* (12), 5232-5238.

(14) Jhang, L.-J.; Wang, D.; Silver, A.; Li, X.; Reed, D.; Wang, D. Stable all-solid-state sodium-sulfur batteries for low-temperature operation enabled by sodium alloy anode and confined sulfur cathode. *Nano Energy* **2023**, *105*, 107995.

(15) Yu, X.; Manthiram, A. Capacity Enhancement and Discharge Mechanisms of Room-Temperature Sodium–Sulfur Batteries. *ChemElectroChem* **2014**, *1* (8), 1275-1280.

(16) Ji, T.; Tu, Q.; Zhao, Y.; Wierzbicki, D.; Plisson, V.; Wang, Y.; Wang, J.; Burch, K. S.; Yang, Y.; Zhu, H. Three-step thermodynamic vs. two-step kinetics-limited sulfur reactions in all-solid-state sodium batteries. *Energy & Environmental Science* **2024**.

(17) Tian, Y.; Shi, T.; Richards, W. D.; Li, J.; Kim, J. C.; Bo, S.-H.; Ceder, G. Compatibility issues between electrodes and electrolytes in solid-state batteries. *Energy & Environmental Science* **2017**, *10* (5), 1150-1166.

(18) Li, Y.; Tang, Y.; Li, X.; Tu, W.; Zhang, L.; Huang, J. In Situ TEM Studies of Sodium Polysulfides Electrochemistry in High Temperature Na–S Nanobatteries. *Small* **2021**, *17* (23), 2100846.

(19) Nikiforidis, G.; Van de Sanden, M.; Tsampas, M. N. High and intermediate temperature sodium–sulfur batteries for energy storage: development, challenges and perspectives. *RSC advances* **2019**, *9* (10), 5649-5673.

(20) Wan, B.; Xu, S.; Yuan, X.; Tang, H.; Huang, D.; Zhou, W.; Wu, L.; Zhang, J.; Gou, H. Diversities of stoichiometry and electrical conductivity in sodium sulfides. *Journal of Materials Chemistry A* **2019**, *7* (27), 16472-16478.

(21) Böttcher, P. Zur Kenntnis der Verbindung Na2S3. *Zeitschrift für anorganische und allgemeine Chemie* **1980**, *467* (1), 149-157.

(22) Tan, C.; Heenan, T. M.; Ziesche, R. F.; Daemi, S. R.; Hack, J.; Maier, M.; Marathe, S.; Rau, C.; Brett, D. J.; Shearing, P. R. Four-dimensional studies of morphology evolution in lithium–sulfur batteries. *ACS Applied Energy Materials* **2018**, *1* (9), 5090-5100.

(23) Risse, S.; Jafta, C.; Yang, Y.; Kardjilov, N.; Hilger, A.; Manke, I.; Ballauff, M. Multidimensional operando analysis of macroscopic structure evolution in lithium sulfur cells by X-ray radiography. *Physical Chemistry Chemical Physics* **2016**, *18* (15), 10630-10636.

(24) Yang, H.; Gao, M.; Zhou, X.; Duan, D.; Cao, J.; Liu, S. Accelerating Na2S/Na2S2 conversion kinetics by electrolyte additive with high Na2S/Na2S2 solubility for high-performance room-temperature sodium–sulfur batteries. *Journal of Power Sources* **2024**, *606*, 234592.

(25) Zhang, B.-W.; Sheng, T.; Liu, Y.-D.; Wang, Y.-X.; Zhang, L.; Lai, W.-H.; Wang, L.; Yang, J.; Gu, Q.-F.; Chou, S.-L. Atomic cobalt as an efficient electrocatalyst in sulfur cathodes for superior room-temperature sodium-sulfur batteries. *Nature communications* **2018**, *9* (1), 4082.

(26) Ye, C.; Jiao, Y.; Chao, D.; Ling, T.; Shan, J.; Zhang, B.; Gu, Q.; Davey, K.; Wang, H.; Qiao, S. Z. Electron-state confinement of polysulfides for highly stable sodium–sulfur batteries. *Advanced Materials* **2020**, *32* (12), 1907557.

(27) Kim, J. T.; Rao, A.; Nie, H.-Y.; Hu, Y.; Li, W.; Zhao, F.; Deng, S.; Hao, X.; Fu, J.; Luo, J. Manipulating Li2S2/Li2S mixed discharge products of all-solid-state lithium sulfur batteries for improved cycle life. *Nature Communications* **2023**, *14* (1), 6404.

(28) Cao, D.; Sun, X.; Li, F.; Bak, S. M.; Ji, T.; Geiwitz, M.; Burch, K. S.; Du, Y.; Yang, G.; Zhu, H. Understanding electrochemical reaction mechanisms of sulfur in all-solid-state batteries through Operando and theoretical studies. *Angewandte Chemie International Edition* **2023**, *62* (20), e202302363.

(29) Davis, A. L.; Goel, V.; Liao, D. W.; Main, M. N.; Kazyak, E.; Lee, J.; Thornton, K.; Dasgupta, N. P. Rate limitations in composite solid-state battery electrodes: revealing heterogeneity with operando microscopy. *ACS Energy Letters* **2021**, *6* (8), 2993-3003.

(30) Stavola, A. M.; Sun, X.; Guida, D. P.; Bruck, A. M.; Cao, D.; Okasinski, J. S.; Chuang, A. C.; Zhu, H.; Gallaway, J. W. Lithiation Gradients and Tortuosity Factors in Thick NMC111-Argyrodite Solid-State Cathodes. *ACS Energy Letters* **2023**, *8* (2), 1273-1280.

(31) Nguyen, H.; Banerjee, A.; Wang, X.; Tan, D.; Wu, E. A.; Doux, J.-M.; Stephens, R.; Verbist, G.; Meng, Y. S. Single-step synthesis of highly conductive Na3PS4 solid electrolyte for sodium all solid-state batteries. *Journal of Power Sources* **2019**, *435*, 126623.

(32) Duchene, L.; Kuhnel, R. S.; Rentsch, D.; Remhof, A.; Hagemann, H.; Battaglia, C. A highly stable sodium solid-state electrolyte based on a dodeca/deca-borate equimolar mixture. *Chem Commun (Camb)* **2017**, *53* (30), 4195-4198. DOI: 10.1039/c7cc00794a  From NLM PubMed-not-MEDLINE.

(33) Tanibata, N.; Matsuyama, T.; Hayashi, A.; Tatsumisago, M. All-solid-state sodium batteries using amorphous TiS3 electrode with high capacity. *Journal of Power Sources* **2015**, *275*, 284-287.

(34) Kieffer, J.; Karkoulis, D. PyFAI, a versatile library for azimuthal regrouping. In *Journal of Physics: Conference Series*, 2013; IOP Publishing: Vol. 425, p 202012.

(35) Ashiotis, G.; Deschildre, A.; Nawaz, Z.; Wright, J. P.; Karkoulis, D.; Picca, F. E.; Kieffer, J. The fast azimuthal integration Python library: pyFAI. *Journal of applied crystallography* **2015**, *48* (2), 510-519.

(36) Dyadkin, V.; Pattison, P.; Dmitriev, V.; Chernyshov, D. A new multipurpose diffractometer PILATUS@ SNBL. *Journal of synchrotron radiation* **2016**, *23* (3), 825-829.

(37) Ravel, B.; Newville, M. ATHENA, ARTEMIS, HEPHAESTUS: data analysis for X-ray absorption spectroscopy using IFEFFIT. *Journal of synchrotron radiation* **2005**, *12* (4), 537-541.

(38) Okamoto, H. The Li-S (lithium-sulfur) system. *Journal of phase equilibria* **1995**, *16*, 94-97.

(39) Sangster, J.; Pelton, A. The Na-S (sodium-sulfur) system. *Journal of phase equilibria* **1997**, *18* (1), 89-96.

(40) Gu, J.; Hu, W.; Wu, Y.; Ren, F.; Liang, Z.; Zhong, H.; Zheng, X.; Ma, R.; Luo, Y.; Chen, X. Asymmetric Sulfur Redox Paths in Sulfide-Based All-Solid-State Lithium–Sulfur Batteries. *Chemistry of Materials* **2024**, *36* (9), 4403-4416.

(41) Xiao, Y.; Yamamoto, K.; Matsui, Y.; Watanabe, T.; Sakuda, A.; Nakanishi, K.; Uchiyama, T.; Hayashi, A.; Shingubara, S.; Tatsumisago, M. Comparison of sulfur cathode reactions between a concentrated liquid electrolyte system and a solid-state electrolyte system by soft X-ray absorption spectroscopy. *ACS Applied Energy Materials* **2020**, *4* (1), 186-193.

(42) Takeuchi, T.; Kageyama, H.; Nakanishi, K.; Tabuchi, M.; Sakaebe, H.; Ohta, T.; Senoh, H.; Sakai, T.; Tatsumi, K. All-solid-state lithium secondary battery with Li2S–C composite positive electrode prepared by spark-plasma-sintering process. *Journal of The Electrochemical Society* **2010**, *157* (11), A1196.

(43) Manthiram, A.; Yu, X. Ambient temperature sodium–sulfur batteries. *small* **2015**, *11* (18), 2108-2114.
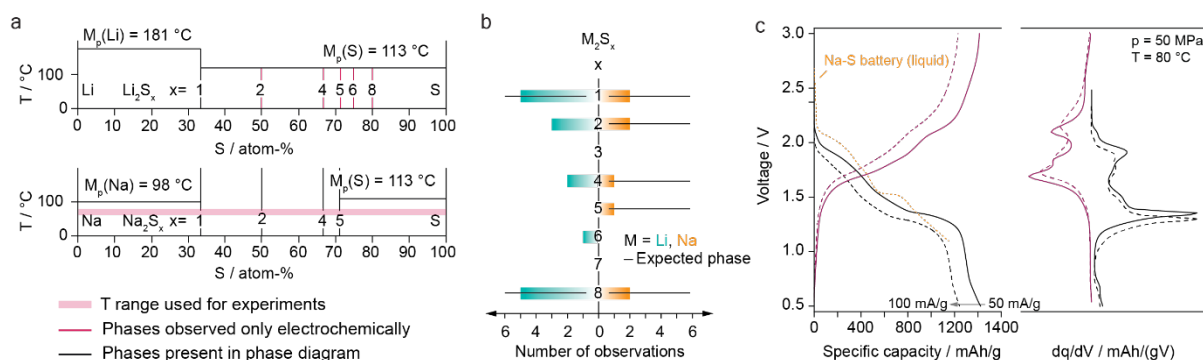
# Figures



**Figure 1 | Phase behavior of M-S systems and comparison with experimental electrochemical measurements.** (a) Zoomed-in phase diagrams of the Li-S (a)[38] and Na-S (b)[39] systems, showing the relevant temperature ranges, excluding regions containing liquid phases. The pink-shaded area represents the temperature range used in this study to investigate polysulfide formation. (b) Schematic depicting the theoretically possible polysulfides ($M_2S_x$, with M = Li, Na, and $x \in \{1, 2, ..., 8\}$)[25], and the frequency of observation of these polysulfides in M-S solid-state batteries with inorganic electrolytes.[13, 16, 27, 28, 40-42] (c) Voltage profile and corresponding dq/dV plot for $Na_{15}Sn_4$(80:20) | $Na_3PS_4$ | S (33%)/C (17%)/$Na_3PS_4$ (33:17:50) with an areal loading of 3.6 mAh/cm², measured at two different rates (50 mAh/g and 100 mAh/g, the latter used for operando XRD), compared with the voltage profile of a conventional Na-S battery.[43]
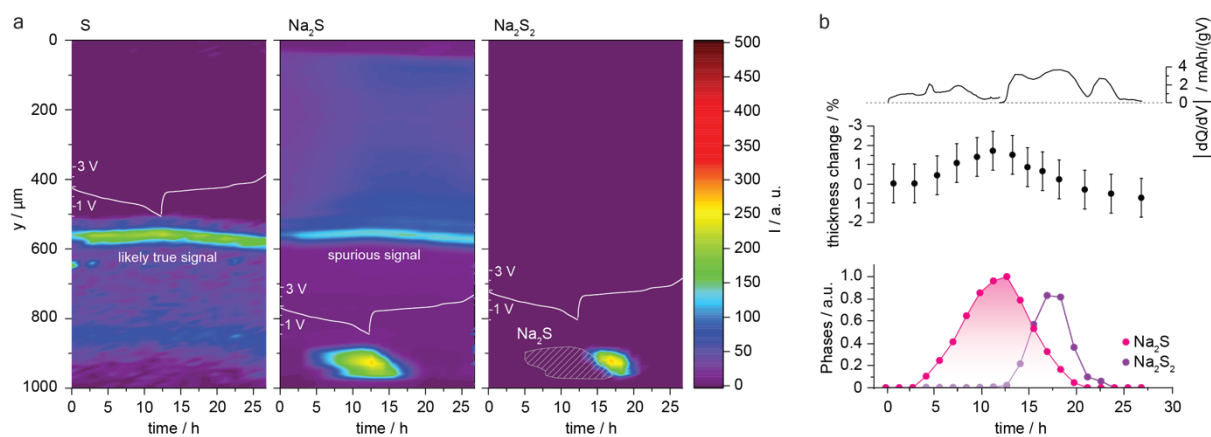
**Figure 2 | Spatial and time-resolved XRD analysis.** (a) Phase maps of the individual compounds: orthorhombic sulfur (S), cubic Na₂S, and rhombohedral Na₂S₂, along with the corresponding voltage profile. The only observable phases are crystalline polysulfides, with sulfur remaining mostly undetectable throughout the experiment. (b) Compositional changes across the cross-section over time, correlated with the thickness variation of the composite cathode and synchronized with the dq/dV plot. Not all peaks in the dq/dV plot align with the phases formed during charge and discharge, suggesting the presence of non-crystalline phases.
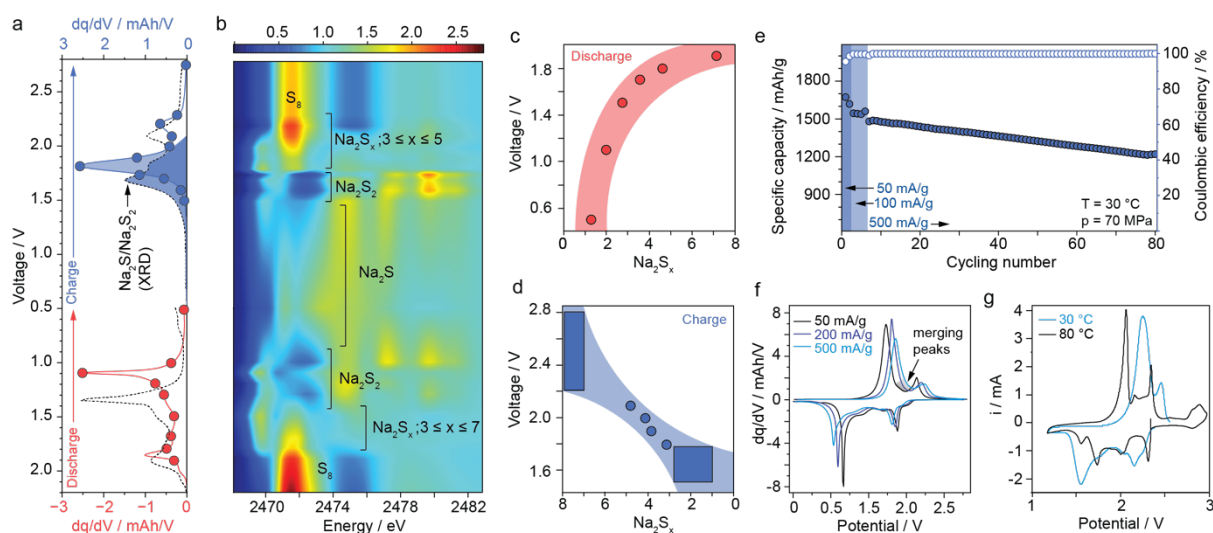
19

**Figure 3 | Ex-situ soft XAS and electrochemical analysis** (a) dq/dV plot of solid-state Na-S battery employing $Na_3PS_4$ (80 °C; dashed line) or $Na_4(B_{10}H_{10})(B_{12}H_{12})$ (30 °C; solid line). Red and blue dots indicated the voltage where individual cells had been stopped for XAS studies. Blue highlighted peaks indicate the merging of two contributions to do changing kinetics. (b) Contour plot of the ex-situ XAS of the solid-state Na-S battery, showing the discharge cycle and charging cycle. Highlighted regions showing the corresponding XAS spectra of the different polysulfides, grouping the high-ordered $Na_xS_x$; x=[3:7]. (c) Formation plot of the different polysulfides in during discharge and (d) charge, showing the formation voltage v. sodiation (e) Cycling performance of the solid-state Na-S battery employing $Na_4(B_{10}H_{10})(B_{12}H_{12})$ at a rate of 500 mA/g, with a few formation cycles at rates of 50 and 200 mAh/g to ensure proper formation of battery's internal structure and chemistry. (f) Selected dQ/dV plot based on (e) for 50, 200, and 500 mA/g. The arrow indicates peak merging with higher current densities. (g) Cyclic voltammogram of solid-state Na-S battery employing $Na_4(B_{10}H_{10})(B_{12}H_{12})$ at 30 °C and 80 °C, scanned at 25 µV/s and 10 mV/s respectively.
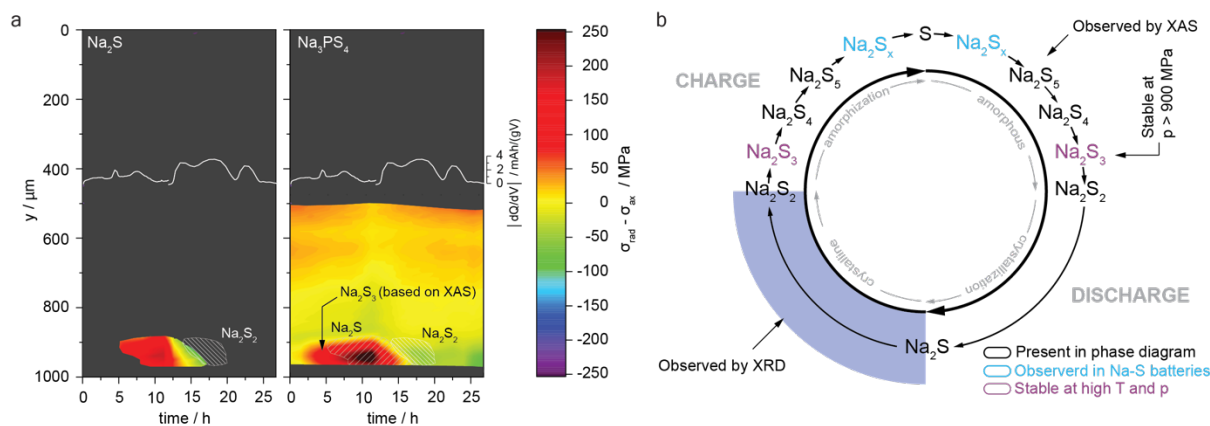
20

**Figure 4 | Stress profile analysis derived from diffraction data and proposed reaction mechanism.** (a) Time-dependent evolution of stress profiles across the cross-section of the cell during charge and discharge, shown alongside the corresponding differential voltage profile. Stress was calculated using the (100) and (101) diffraction peaks of $Na_2S$ and $Na_3PS_4$, respectively. Crystalline phases identified in Figure 2, namely $Na_2S$ and $Na_2S_2$, are highlighted by shaded areas. Notably, significant stress is generated prior to the formation of crystalline phases, indicating the presence of additional amorphous polysulfides. (b) Summary of reaction pathway during charge and discharge.